This article has been accepted for publication in a future issue of this journal, but has not been fully edited. Content may change prior to final publication. Citation information: DOI 10.1109/TBME.2019.2897935, IEEE Transactions on Biomedical Engineering

Electrode-Electrolyte Interface Modeling and Impedance Characterizing of Tripolar Concentric Ring Electrode

Seyed Hadi Nasrollaholhosseini, *Student Member, IEEE,* Jason Mercier, Godi Fischer, *Life Time Memebr, IEEE* and Walter G. Besio, *Senior Memebr, IEEE*

***Abstract*—Electrodes are used to convert ionic currents to electrical currents in biological systems. Modeling the electrode-electrolyte interface and characterizing the impedance of the interface could help to optimize the performance of the electrode interface to achieve higher signal to noise ratios. Previous work has yielded accurate models for single-element biomedical electrodes. This paper introduces a model for a tripolar concentric ring electrode (TCRE) derived from impedance measurements using electrochemical impedance spectroscopy (EIS) with a Ten20 electrode impedance matching paste. It is shown that the model serves well to predict the performance of the electrode-electrolyte interface for TCREs as well as standard cup electrodes. In this paper we also discuss the comparison between the TCRE and the standard cup electrode regarding their impedance characterization and demonstrate the benefit of using TCREs in biomedical applications. We have also conducted auditory evoked potential experiments using both TCRE and standard cup electrodes. The results show that EEG recorded from tripolar concentric ring electrodes (tEEG) is beneficial, acquiring the auditory brainstem response (ABR) with less stimuli with respect to recoding EEG using standard cup electrodes.**

***Index Terms*—Tripolar concentric ring electrode, spectroscopy, electrode-electrolyte interface, double layer capacitance.**

I. Introduction

PHYSIOLOGICAL systems such as the cardiovascular system, the nervous system, and the muscular system all generate ionic current flows in the body. Each physiological process is associated with specific signals that reflect the underlying nature and activities of each source. Biomedical signals can be obtained with electrodes that measure local electrical activities generated by physiological processes. One such biomedical signal of interest is the electroencephalography (EEG) signal revealing electrical activity of the brain.

The electrodes convert the ionic currents generated by the underlying cells of the human body into electrical currents [1]. In essence, they act as transducers between ionic and electronic currents. A mathematical model of the electrode, electrolyte, and body may help us to have a better understanding of how electrodes record biomedical signals. Since electrodes act as transducers, we need to understand the mechanisms that generate the transduction process between the electrode and the human body. Moreover, physiological processes in the human body generate ionic current flows in the volume conductor, the body. Hence, an electrode-electrolyte interface forms the contact site of an electrode to the body. Figure 1 illustrates the contact of an electrode to an electrolyte. At the interface of electrode-electrolyte, electrochemical reactions take place that can be described by the following equations [2]:

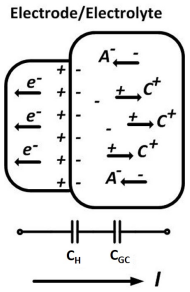

Fig. 1. Electrode-Electrolyte Interface

$$C \Leftrightarrow C^{n+} + ne^- \quad (1)$$

$$A^{m-} \Leftrightarrow A + me^- \quad (2)$$

Equation (1) describes the oxidation reaction from left to right, and the reduction reaction from right to left, and both reduction and oxidation can occur at the electrode-electrolyte interface. It also reveals that for an efficient electron-ion exchange at the interface, we should place a metal (C) into an aqueous solution containing ions of the metal (C+). Thus, oxidation causes cations to be dispersed into the electrolyte and electrons to be left in the electrode. Equation (2) shows that the anions (A) can also be oxidized to a neutral atom and release one or more electrons by moving to the interface.

Obtaining an accurate model for the electrode-electrolyte interface is an on-going research topic, which has been studied for many years. The electric double layer (EDL) concept was first proposed by Helmholtz in 1879 [3]. He found that at the electrode-electrolyte interface, since the electrolyte is saturated with charged electrons, the coions will be pushed back while the counterions will be attracted. Therefore, there will be two compact layers of opposite charges at the electrode-electrolyte interface called the electric double layer. More specifically, an

Research was partially supported by NSF awards 1539068 and 1430833 to WB and do not reflect the views of NSF. The content is solely the responsibility of the authors and does not necessarily represent the official views of the National Science Foundation.

S. H. Nasrollaholhosseini, J. Mercier, G. Fischer and Walter G. Besio (e-mail: besio@uri.edu) are with the Electrical, Computer, and Biomedical Engineering Department, University of Rhode Island, Kingston, RI 02881 USA.

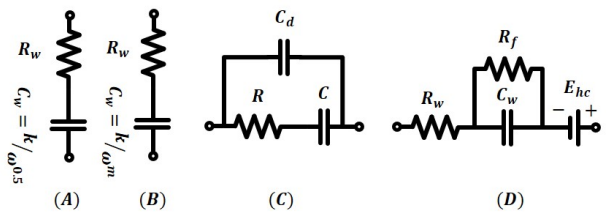

Fig. 2. Electrical circuit model evolution of the electrode-electrolyte interface. (A) Warburg, (B) Fricke (C) Randles, and (D) Geddes and Baker models

electric double layer is obtained as a series combination of two conventional capacitors consisting of Helmholtz capacitance and the Gouy-Chapman capacitance that are shown in Fig.1 as C_H and C_{GD} respectively and are discussed in detail in III "Equivalent Circuit Model".

Warburg was the first who proposed an electrode-electrolyte model in 1899. His proposed model consists of a series combination of a capacitor, C_W, and resistor, R_W which are shown in Fig. 2A. The reactance and resistance magnitudes are dependent on the electrode type, the area (including surface conduction), the electrolyte, the frequency, and the current density [4]. In the Warburg model R_ω and C_ω were proposed for an infinitely low density current, which decreases as the inverse square root of frequency ($\frac{1}{\sqrt{f}}$).

In 1932, Fricke, suggested a similar model for the electrode-electrolyte interface. He kept the Warburg combination of a series resistor and capacitor but added that $C_\omega = \frac{k}{\omega^m}$. In the Fricke model shown in Fig. 2b, the Warburg reactance and resistance become:

$$X_\omega = \frac{1}{k\omega^{1-m}} \tag{3}$$

$$R_\omega = \frac{X_\omega}{\tan\frac{m\pi}{2}} \tag{4}$$

where k and m depend on the metal species.

Another popular model for the electrode-electrolyte interface was proposed by Randles in 1947 which is illustrated in Fig. 2C. In this model, a double-layer capacitance C_d was added in parallel with a series combination of resistance R and capacitance C. However, the above mentioned models do not consider the direct current (DC) flowing through the interface. In 1968 [4], Geddes and Baker proposed another model that included the passage of a DC current through the interface. In their model, the Warburg capacitance, C_W is connected in parallel with the Faradic resistance, R_f to model the property of DC current through the interface. This model is shown in Fig. 2D.

The exchange of the anions and cations at the interface alters the local concentration of cations and anions. Therefore, the neutrality of charge is altered in the solution. As a result, the electrolyte that is closest to the interface has a different potential with respect to the rest of the electrolyte. This electric potential difference is called the half-cell potential. The half-cell potential is related to the metal, the concentration of ions in the electrolyte, temperature and other second-order factors [2]. When a circuit is constructed to allow current to flow across an electrode-electrolyte interface, the observed half-cell potential is often altered. The difference between the observed half-cell potential for a particular circuit and the standard half-cell potential is known as the overpotential. Three basic mechanisms contribute to the overpotential: ohmic, concentration, and activation [2].

Tripolar concentric ring electrodes (TCREs) consisting of an outer ring, a middle ring, and a central disc (Fig. 5D, 5E), are distinctively different from conventional cup electrodes featuring a single element (Fig. 5A, 5B). TCREs have been shown to reveal the local surface Laplacian directly, the second spatial derivative of the surface potentials [5], a two-dimensional Laplacian algorithm that weights the middle ring and central disc signal difference sixteen times greater than the outer ring and central disc difference [5]. Compared to EEG from conventional cup electrodes, tripolar Laplacian EEGs from TCREs (tEEG) have been shown to feature approximately 2.5 times higher spatial selectivity, 3.7 times higher signal-to noise ratio and about 12 times lower mutual information [6].

In this paper, we measured the impedance on both tripolar concentric ring electrodes and standard cup electrodes by electrochemical impedance spectroscopy (EIS) using the two electrode and three electrode experiments of the Gamry potentiostat. We also predicted the performance by utilizing the model proposed in [7], [8] and compared the theoretical results to the recordings.

The paper is organized as follows. Section II explains the procedure of how the impedance is measured using EIS. The equivalent circuit model for the tripolar concentric ring electrode is addressed in section III. Section IV presents the results and section V draws some conclusions.

II. Procedure

In order to measure impedances on both TCREs and standard cup electrodes, we performed electrochemical impedance spectroscopy (EIS) ten times each, using Ten20 (Weaver Company) as an electrode paste. In the literature the values of scalp conductivity are from 0.25 to 0.44 S/m [9]-[10]. We also measured the conductivity of Ten20 paste and found that it has a similar conductivity as the scalp, ranging approximately 0.32 to 0.44 S/m. Therefore, when we used 1.5cm of Ten20 paste, we assume that first 2-3mm of paste are modeling the electrolyte and the remaining paste is modeling the scalp. For our experiments we applied the paste on to a plastic plate and attached the electrodes directly to the paste in order to mimic the skin-to-electrode contact. To perform EIS measurements, we used the Gamry potentiostatic instrument framework. We set the AC voltage to 10 mV_{rms}. The system was configured in order to perform both two-electrode and Three-electrode measurements.

The Gamry potentiostat we used is a 4-probe instrument. This means there are four relevant leads that need to be placed. The two-electrode set up (as depicted in Fig. 3) allowed us to measure the impedances between the central disc and middle ring (DM) of the TCREs, as well as the impedances between the central disc and outer ring (DO). When measuring the impedance between middle ring and central disc, we connected

This article has been accepted for publication in a future issue of this journal, but has not been fully edited. Content may change prior to final publication. Citation information: DOI 10.1109/TBME.2019.2897935, IEEE Transactions on Biomedical Engineering

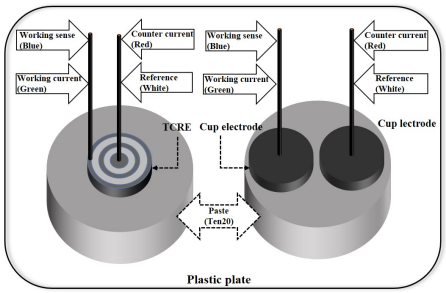

Fig. 3. Two electrode setup of TCRE and conventional cup electrode

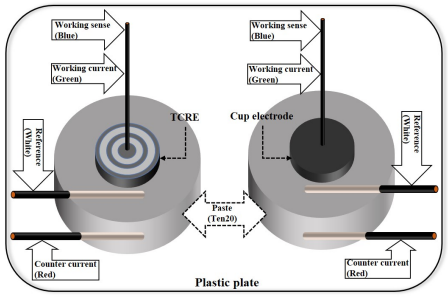

Fig. 4. Three electrode setup of TCRE and conventional cup electrode

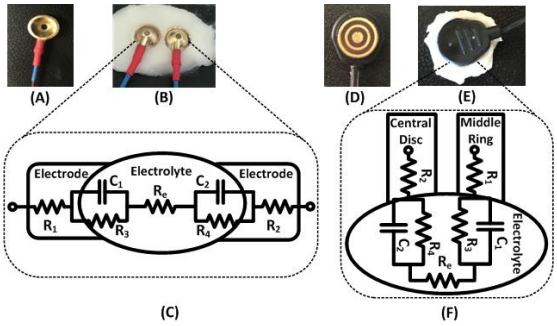

Fig. 5. Disc electrode (A), Disc electrodes placed on Ten20 paste (B), electrical circuit model of the Disc electrode placed on the electrolyte (C), TCRE electrode (D) TCRE placed on Ten20 paste (E), electrical circuit model of the TCRE placed on the electrolyte (F)

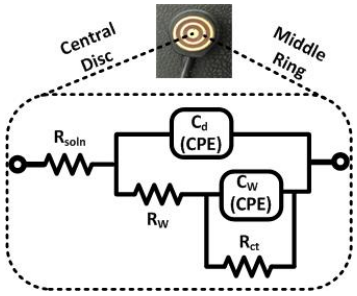

Fig. 6. Electrical model for the tri-polar concentric ring electrode

the blue (working sense) and green (working current) leads to the middle ring and the white (reference) and red (counter current) leads to the central disc. The same setup was used while measuring the impedance between outer ring and central disc, the only difference was the blue and green leads were now connected to the outer ring.

We utilized the three-electrode configuration to measure the impedance of each ring (the central disc, the middle ring and the outer ring) to the electrolyte (as shown in Fig. 4). In this set up, the white lead (reference) is separated from the red lead (counter). When measuring the impedance between the central disc and the electrolyte, the green and blue leads (working and working sense) are attached to the central disc. A copper 15 awg wire is connected to the white lead (reference) and is positioned so that it is measuring a point very close to the working and working sense electrodes. The same type of wire is connected to the red lead (counter) that is placed 1cm away in the paste. To measure the impedances of the middle ring to the electrolyte and the outer ring to the electrolyte, a similar configuration was used, except that the working, and the working sense, leads were now connected to the middle and the outer ring, respectively.

To obtain a reference, we also measured the impedances between two standard cup electrodes in a two electrode set up (as shown in Fig. 3) as well as between the standard cup electrode and the electrolyte in a three electrode configuration (as illustrated in Fig. 4). In the two electrode configuration, the two standard cup electrodes were connected in the same manner with no specification as to which one went to green and blue or white and red leads. The leads were placed as close together as possible on the same span of paste in order to resemble the measurement conditions for the TCRE recordings. Furthermore, in the three electrode configuration, an analogous condition to the TCRE recording was used.

III. Equivalent Circuit Model

Electroencephalography (EEG) is one of the mainstays of hospital diagnostic procedures and pre-surgical planning. Unfortunately, end users frequently struggle with EEGs poor spatial resolution, selectivity and low signal-to-noise ratio, which limits its effectiveness in research, discovery and diagnosis [11]-[12]. Having an outer ring with 4.4mm inner radius, 5mm outer radius, a middle ring with 2.5mm inner radius and 3.2mm outer radius a central disc with 1.4mm radius (Fig. 5D, 5E) renders tripolar concentric ring electrodes (TCREs) distinctively different from conventional cup electrodes (Fig. 5A and 5B). However, the total diameter of both the TCRE and the cup electrode are 10mm and both are gold plated.

Fig. 5A illustrates a conventional cup electrode. Fig. 5B shows the cup electrodes placed in the fresh Ten20 (Weaver and Company) paste similar to real recordings to mimic the body. The equivalent circuit model for this configuration is shown in Fig. 5C. The TCRE electrode in Fig. 5E is placed in fresh Ten20 paste. Therefore, there is an electrode-electrolyte interface between each pair of rings of the TCRE. Fig. 5F illustrates part of the electrical model representation for the TCRE electrode-electrolyte interface between the central disc and middle ring. In both models, as presented above in Fig. 2, R_1, C_1 and R_2, C_2 are the equivalent series resistances and capacitances of the two electrode-electrolyte interfaces. For the TCRE, there will be two more such models: one for the outer ring and central disc, and one for the middle ring and outer ring. R_e represents the electrolyte resistance

and the resistors R_3 and R_4 are the equivalent resistances for the leakage current of the electrode-electrolyte interface, respectively. Therefore, if we neglect R_3 and R_4 at higher frequency, the impedance seen between the middle ring to the central disc Z_{DM} becomes:

$$Z_{DM} = R_1 + \frac{1}{j\omega C_1} + R_e + \frac{1}{j\omega C_2} + R_2 \tag{5}$$

the resistive part in equation (5) is:

$$R_{DM} = R_1 + R_e + R_2 \tag{6}$$

where R_e is an ionic solution resistance, which depends on the ion concentration, ion type, temperature and active cross section. The reactive part in equation (5) is:

$$\frac{1}{C_{DM}} = \frac{1}{C_1} + \frac{1}{C_2} \tag{7}$$

The authors proposed the TCRE model that is depicted in Fig. 6 [7]-[8]. A non-linear least squares fitting program was used to fit the model to the experimental data. The Simplex algorithm in the Echem Analyst was utilized for fitting. The algorithm automatically adjusts the parameter values of the elements in the model to find the best fit. In this model, R_{soln} is the equivalent solution (electrolyte) resistance, C_d represents the equivalent double layer capacitance, R_W and C_W are the equivalent Warburg combination and R_{ct} is the charge-transfer resistance, which represents the equivalent Faradic leakage process in the electrode-electrolyte interface according to [13], [14]:

$$R_{ct} = \frac{kT}{qzJ_0} \tag{8}$$

where k is the Boltzmann constant, T denotes the absolute temperature, q is the electron charge, z denotes the charge on the ion in solution and J_0 represents the equilibrium charge density.

The resistor R_{soln} in the proposed model dominates the impedance at high frequencies. This resistance encompasses all the paths from electrode to electrolyte such as: interconnect resistance and solution or spreading resistance. For a round electrode, its value is [13], [14], [15]:

$$R_{soln} = \frac{\rho}{4r} \tag{9}$$

where r and ρ represent the radius and the solution resistivity respectively.

To match the model perfectly with the experimental data, a constant phase element (CPE) was used instead of capacitors. In fact, double layer capacitors often behave like CPEs rather than pure capacitors [16], [17]. The impedance of a double layer capacitor has the form:

$$Z_{CPE} = \frac{1}{Q(j\omega)^{\alpha}} \tag{10}$$

If $\alpha = 1$, this equation describes a capacitance and Q has units of Farad. If $0 < \alpha < 1$, the equation represent a CPE and Q has units of $Fcm^{-2}s^{(\alpha-1)}$, $\frac{s^{\alpha}}{\Omega}$.

An electric double layer is obtained as a series combination of two capacitances consisting of the Helmholtz capacitance and the Gouy-Chapman capacitance, which is a diffuse layer accounting for the mobility of ions in the electrolyte [3]. In order to relate the potential with the charge distribution, Poisson's equation is used to define the variation of potential (φ) with distance in the Helmholtz layer. Besides, if we assume a one dimensional potential variation in the direction perpendicular to the solid solution interface, we have [3], [13]-[18]:

$$\frac{d^2\varphi}{dx^2} = -\frac{\rho(x)}{\epsilon_0\epsilon_r} \tag{11}$$

where (φ) is the electric potential, ρ is the charge density, ϵ_0 is the permittivity of free space, ϵ_r is the permittivity of the medium and x is the distance from the electrode.

If we consider ions as point charges in the Helmholtz layer, the capacitance per unit surface area of the Helmholtz double layer denoted by C_H becomes [3], [13]-[18]:

$$C_H = \frac{\epsilon_0\epsilon_H}{d_H} \tag{12}$$

where ϵ_H is the relative permittivity of the Helmholtz plane and d_H the distance of the Helmholtz plane to the electrode. d_H can be approximated as the radius of solvated ions.

Gouy and Chapman modified the double layer electrode model, which is shown in Fig. 1 as C_{GC}, by also taking into account the mobility of ions in the solution. An accumulation of oppositely charged ions will be outside the Helmholtz layer. The distribution of ions is given by the Boltzmann distribution [3]:

$$n_i = n_i^{\infty} exp(-\frac{z_i e\varphi}{kT}) \tag{13}$$

where n_i is the ions concentration of type i per unit volume near the interface, n_i^{∞} the concentration of ions of type i per unit volume in the bulk solution, e the electronic charge, z_i the charge on the ion i, k the Boltzmann constant and T the absolute temperature.

The total charge density per unit volume for all ionic species is given by the sum over all ions:

$$\rho = \sum_i z_i e n_i = \sum_i z_i e n_i^{\infty} exp(-\frac{z_i e\varphi}{kT}) \tag{14}$$

The Poisson-Boltzmann equation is obtained by combining equations (11) and (14):

$$\frac{d^2\varphi}{dx^2} = -\frac{e}{\epsilon_0\epsilon_r}\sum_i z_i n_i^{\infty} exp(-\frac{z_i e\varphi}{kT}) \tag{15}$$

By multiplying both sides of equation (15) by $2\frac{dy}{dx}$, and solving for a planar electrode considering the boundary conditions: (1) $\varphi(0) = \varphi_0$ and (2) $\varphi(\infty) = 0$ and solved further for a symmetrical electrolyte yields:

$$\frac{d\varphi}{dx} = \sqrt{\frac{2kTn^{\infty}}{\epsilon_r\epsilon_0}}\left[exp(-\frac{ze\varphi_d}{2kT}) - exp(\frac{ze\varphi_d}{2kT})\right] \tag{16}$$

If σ_d is the charge density of the diffused layer expressed in C/m^2 then,

$$\sigma_d = -\epsilon_r \epsilon_0 \frac{d\varphi}{dx} \mid_{x=0} \tag{17}$$

The charge density of the diffused layer can be derived from equations (16) and (17) and becomes,

$$\begin{aligned} \sigma_d &= -\epsilon_r \epsilon_0 \frac{d\varphi}{dx} \mid_{x=0} \\ &= \sqrt{2kTn^{\infty}\epsilon_r\epsilon_0}\left[exp(\frac{ze\varphi_d}{2kT}) - exp(-\frac{ze\varphi_d}{2kT})\right] \\ &= \sqrt{8kTn^{\infty}\epsilon_r\epsilon_0}\ \sinh\left(\frac{ze\varphi_d}{2kT}\right) \end{aligned} \tag{18}$$

Finally, the differential Gouy-Chapman capacitance is obtained by differentiating equation (17) [3], [18],

$$C_{GC} = \frac{d\sigma_d}{d\varphi_0} = \sqrt{\frac{2z^2e^2n^{\infty}\epsilon_r\epsilon_0}{kT}}\ \cosh\left(\frac{ze\varphi_d}{2kT}\right) \tag{19}$$

Therefore, the double layer capacitance that occurs at the electrode-electrolyte interface is the series combination of the Helmholtz capacitance and the Gouy-Chapman capacitance. This combination model is given by Stern and is called "Gouy-Chapman-Stern" model and can be written as [3], [13]-[18]:

$$\frac{1}{C_{dl}} = \frac{1}{C_H} + \frac{1}{C_{GC}} \tag{20}$$

IV. Auditory Evoked Potential

Evoked potentials are the brains electrical activity recorded in response to a stimulation of one of the body's sensory mechanisms. The early component of the overall auditory evoked potential (AEP) is the auditory brain stem response (ABR) which can be recorded from the electrodes placed on the scalp of a subject [19]-[20]. The ABR has a very low amplitude. Therefore, to extract the ABR from background EEG, repeated trials are averaged synchronized to the stimulus. The averaging technique improves the signal-to-noise ratio of the ABR significantly. This technique employs about 2000-3000 responses which have the same time window to the stimulus [19]-[21]. Thus, signal averaging can be very time consuming and uncomfortable for both clinicians and subjects. Reducing the required number of trials would be of great significance. In this test, a Brain Products V-Amp and Recorder software was used to record the tEEG and EEG signals simultaneously with the sampling rate of 20,000 Hz. The intensity of the audio cue was adjusted to 70dB and a frequency of 4 kHz with a duration of 1.0 ms that was repeated at 39.1 Hz was provided. The participant listened to 100 consecutive audio cues followed by a rest pause and then repeated ten times for a total of 1000 audio cues.

The participants (n=6, 2 female) were all healthy and signed URI IRB approved consents and sat in a comfortable position in front of the computer screen and had TCREs placed at position C_z and the right mastoid, with a reference cup electrode placed on the left mastoid and a ground cup electrode placed on the mid-forehead. The impedances between the TCREs and reference cup electrode was below $10k\Omega$ for each participant. Audio cues were provided to the right ear with an earbud. Testing was performed in a quiet, but not sound–shielded room, with eyes closed. During the breaks, participants could open their eyes and adjust their position if needed. The computer monitor showed a countdown clock of pending audio cues. The ABRs data for this study were bandpass filtered at 300-900 Hz (Butterworth forward and backward) and epoch windowed between -5 ms prior to, and up to 15 ms after the stimuli.

V. Results

EIS: The Bode plots resulting from the two electrode set up for the TCRE between central disc to middle ring (DM) and central disc to outer ring (DO) using the Ten20 paste are shown in Fig. 7 and Fig. 8, respectively. Figures 9-11 depict the Bode plots measuring the impedances of each ring (central disc, middle and outer ring) to the electrolyte utilizing three electrode configuration. In each setup, 10 experiments were conducted in order to reduce nuisance variables such as environmental noise. In each figure, the top plot shows the results of 10 different experiments in which the average of

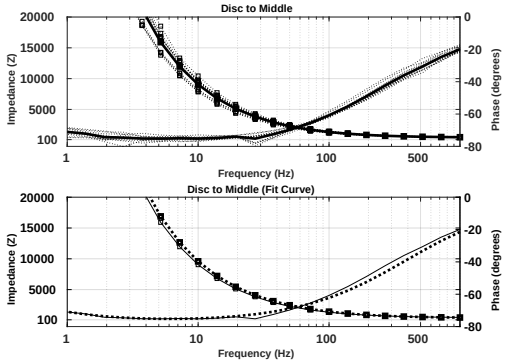

Fig. 7. Bode plots of the TCRE for the central disc to middle ring (DM) with 10 different experiments with the averaged data is shown in bold (top). The curve fit is shown with a dashed bold trace and the averaged data is shown in the solid trace (bottom). In each figure, the impedance curves are specified with squares.

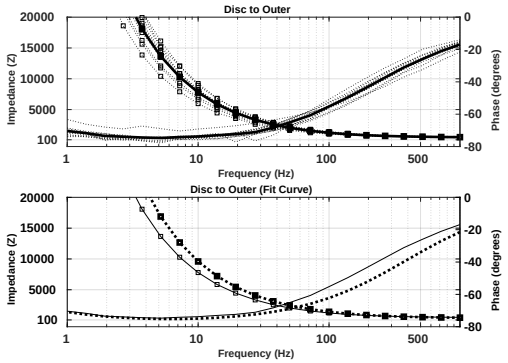

Fig. 8. Bode plots of the TCRE for the central disc to outer ring (DO) with 10 different experiments with the averaged data is shown in bold (top). The curve fit is shown with a dashed bold trace and the averaged data is shown in the solid trace (bottom). In each figure, the impedance curves are specified with squares.

This article has been accepted for publication in a future issue of this journal, but has not been fully edited. Content may change prior to final publication. Citation information: DOI 10.1109/TBME.2019.2897935, IEEE Transactions on Biomedical Engineering

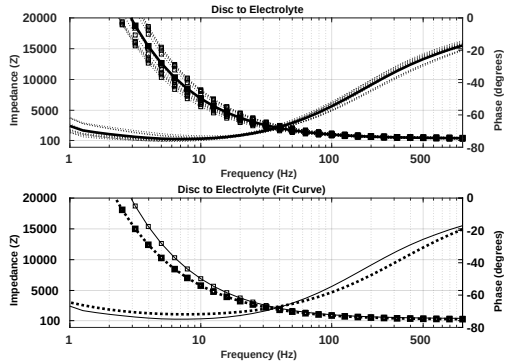

Fig. 9. Bode plots of the TCRE for the central disc to electrolyte with 10 different experiments with the averaged data is shown in bold (top). The curve fit is shown with a dashed bold trace and the averaged data is shown in the solid trace (bottom). In each figure, the impedance curves are specified with squares.

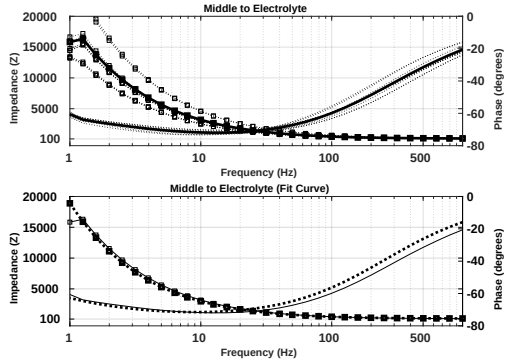

Fig. 10. Bode plots of the TCRE for the middle ring to electrolyte with 10 different experiments with the averaged data is shown in bold (top). The curve fit is shown with a dashed bold trace and the averaged data is shown in the solid trace (bottom). In each figure, the impedance curves are specified with squares.

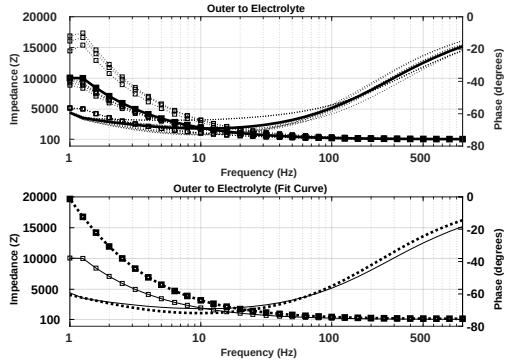

Fig. 11. Bode plots of the TCRE for the outer ring to electrolyte with 10 different experiments with the averaged data is shown in bold (top). The curve fit is shown with a dashed bold trace and the averaged data is shown in the solid trace (bottom). In each figure, the impedance curves are specified with squares.

these ten experiments is represented in bold. Moreover, the bottom plot in each figure shows the linear curve fits derived from the model for the TCRE that is shown with a dashed bold trace as well as the averaged curves that are plotted with

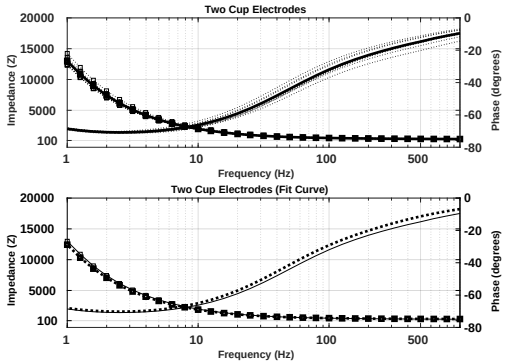

Fig. 12. Bode plots of two standard cup electrodes and electrolyte in between with 10 different experiments with the averaged data is shown in bold (top). The curve fit is shown with a dashed bold trace and the averaged data is shown in the solid trace (bottom). In each figure, the impedance curves are specified with squares.

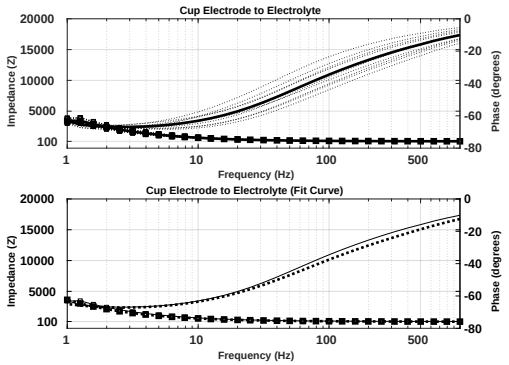

Fig. 13. Bode plots of the standard cup electrode to electrolyte with 10 different experiments with the averaged data is shown in bold (top). The curve fit is shown with a dashed bold trace and the averaged data is shown in the solid trace (bottom). In each figure, the impedance curves are specified with squares.

a solid trace. Besides, in each figure, the impedance curves are specified with squares. The model illustrated in Fig. 6 was used for the linear curve fit. It can be seen from Fig. 7 through Fig. 11 that the fitted curve matches the averaged curve at the interested frequency range of 1Hz to 1kHz very well. Therefore, the model in Fig. 6 can predict the performance of the TCRE accurately.

Figure 12 shows the standard cup electrode Bode plots using the two electrode set up and the same Ten20 paste. The results for the standard cup electrode using the three electrode set up are depicted in Fig. 13. In each case, the top plot shows the ten experiments with the average in bold as well as the linear curve fit using the model of Fig. 6 with the averaged curve in the bottom plot. It can also be deduced from Fig. 12 and Fig. 13 that the model of Fig. 6 predicts the behavior of the standard cup electrode equally well.

When inspecting Fig. 7, through Fig. 13, we notice: (1) the TCRE phase only changes from -70 to -60 degrees with the Ten20 paste in the frequency band $1Hz$ to $100Hz$ while the standard cup electrode phase varies from -75 to -35 degrees. This shows that TCREs are more robust for phase analysis.

This article has been accepted for publication in a future issue of this journal, but has not been fully edited. Content may change prior to final publication. Citation information: DOI 10.1109/TBME.2019.2897935, IEEE Transactions on Biomedical Engineering

TABLE I
PARAMETER VALUES FOR THE TEEG MODEL

Parameters	TCRE (Disc to Middle)	TCRE (Disc to Outer)	TCRE (Disc to Electrolyte)	TCRE (Middle to Electrolyte)	TCRE (Outer to Electrolyte)	Standard Disc to Standard Disc	Standard Disc to Electrolyte
$\mathbf{R_{soln}}(\Omega)$	397.4 ± 3.5	435.3 ± 3.9	292.6 ± 2.2	179.4 ± 1.7	204.6 ± 1.5	351.9 ± 2.7	110.2 ± 1.2
$\mathbf{R_{ct}}(\Omega)$	$2.0e+5$ $\pm 0.5e+5$	$4.2e+5$ $\pm 1.5e+5$	$119.3e+3$ $\pm 235.9e+3$	$98.8e+3$ $\pm 5.0e+3$	$49.6e+3$ $\pm 17.4e+3$	$95.3e+3$ $\pm 6.7e+3$	$23.7e+3$ $\pm 1.4e+3$
$\mathbf{R_w}(\Omega)$	$5.4e+5$ $\pm 0.3e+5$	$3.1e+5$ $\pm 1.2e+5$	$179.7e+3$ $\pm 23.7e+3$	$112.6e+3$ $\pm 16.7e+3$	$49.3e+3$ $\pm 8.3e+3$	$1.1e+3$ $\pm 0.7e+3$	$0.2e+3$ $\pm 0.3e+3$
$\mathbf{C_w}(\frac{s^\alpha}{\Omega})$	$21.6e-6$ $\pm 10.9e-6$	$2.9e-6$ $\pm 2.0e-6$	$14.6e-6$ $\pm 4.5e-6$	$9.0e-6$ $\pm 3.7e-6$	$10.9e-6$ $\pm 2.2e-6$	$1.6e-6$ $\pm 1.3e-6$	$23.7e-6$ $\pm 40.1e-6$
$\alpha_\mathbf{W}$	$999e-3$ $\pm 166.0e-3$	$626.0e-3$ $\pm 158.0e-3$	$999e-3$ $\pm 629.8e-3$	$745.1e-3$ $\pm 84.7e-3$	$911.5e-3$ $\pm 196.8e-3$	$999.0e-3$ $\pm 103.8e-3$	$808.5e-3$ $\pm 135.9e-3$
$\mathbf{C_d}(\frac{s^\alpha}{\Omega})$	$28.7e-7$ $\pm 0.5e-7$	$30.6e-7$ $\pm 1.1e-7$	$51.9e-7$ $\pm 1.2e-7$	$24.2e-7$ $\pm 0.04e-7$	$82.4e-7$ $\pm 2.9e-7$	$148.6e-7$ $\pm 15.9e-7$	$343.4e-7$ $\pm 39.3e-7$
$\alpha_\mathbf{d}$	$870.0e-3$ $\pm 3.4e-3$	$868.0e-3$ $\pm 5.9e-3$	$848.2e-3$ $\pm 4.3e-3$	$999.0e-3$ $\pm 155.2e-3$	$877.4e-3$ $\pm 5.9e-3$	$832.4e-3$ $\pm 10.4e-3$	$843.8e-3$ $\pm 127.5e-3$

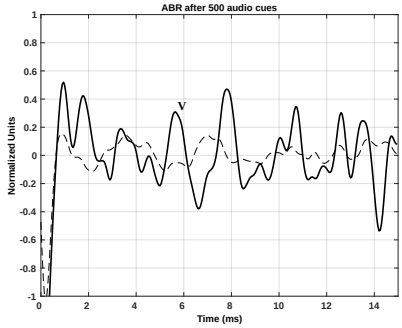

Fig. 14. tEEG (solid bolded traces) vs. EEG (dotted trace) after 500 audio cues.

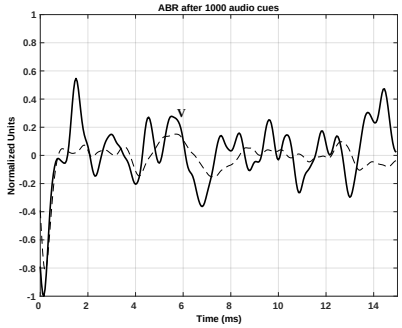

Fig. 15. tEEG (solid bolded traces) vs. EEG (dotted trace) after 1000 audio cues.

(2) the impedance values between the TCRE electrodes are generally higher than between two standard cup electrodes. They are below $10k\Omega$ only from $10Hz$ and beyond, whereas the standard cup electrode impedance is below $5k\Omega$ beyond $3Hz$. (3) The impedance of the center disc to electrolyte is greater than the impedance between middle ring to electrolyte and outer ring to electrolyte. Furthermore, the impedance of the middle ring to electrolyte is greater than the outer ring to electrolyte impedance. (4) the impedance between each ring to electrolyte is smaller than the impedances between central disc to middle and central disc to outer ring in the frequency range $1Hz$ to $100Hz$. This shows that the three rings of the TCREs are not shorted in this frequency range. (5) the impedance between cup electrode to electrolyte is smaller than the impedances between two cup electrodes. Table 1 lists the averaged, fitted parameter values of the equivalent circuit model depicted in Fig. 6 with the corresponding standard deviations for disc to middle ring, disc to outer ring, disc, middle, and outer rings to electrolyte as well as standard cup electrode to standard cup electrode and standard cup electrode to electrolyte using the Ten20 paste.

C_W and C_d are representing the constant phase elements that are used instead of conventional capacitances in the model of Fig. 6 to match the model perfectly with the experimental data. In Table I if the α_W and α_d are 1 the unit of C_W and C_d, as it is described in equation 10, are in F, and the value would be as described in equation 20. With the paste, the parameter values R_{soln}, n, and m were similar for TCREs. The standard deviation for R_{soln}, n, and m, C_d are less than 10% in almost all cases. However, in some cases the variation for R_w, R_{ct}, and C_w, C_d are higher. This might be due to the sensitivity of these parameters with regard to the electrode-electrolyte interface condition.

ABR: The participants all tolerated the experiment. Wave V latency consistently revealed ABR responses at varying stimulation rates and is widely used to detect and mark auditory brainstem responses [19]-[21]. It has been shown that the wave V is identified as the peak near 6 ms after the stimulus onset and immediately before the negative slope [19]-[21]. Wave V has been attributed to activity in the lateral lemniscus and inferior colliculus. Fig. 14 depicts the ABR of the tEEG and EEG with 500 stimuli. Most of the ABR waves are becoming evident in the tEEG (solid trace), although not fully defined. It is not possible to tell if there is an ABR response in the EEG (dash-dotted trace). In Figure 15, after 1000 auditory stimuli, the ABR waves are well defined for the

tEEG (solid bold trace). However, even after 1000 auditory stimuli there still is no evident ABR waves in the EEG (dash-dotted trace).

VI. Conclusion

The goal of this study was to use EIS to enhance our understanding of the physical processes determining the electrode-electrolyte interface with a focus on TCREs and to find an appropriate model, which can be used to improve the interface design. EIS has been utilized to analyze the behavior of the TCRE and the cup electrode, and an equivalent circuit model was used to describe and quantify the electrode-electrolyte interface impedance. The good match between the experimental results and fitted curves derived from an equivalent circuit model shows that the model predicts the behavior of the TCREs very well. Moreover, equations are presented to describe the physical process of the electrode-electrolyte interface. We found that the impedance between the electrodes of the TCREs decreases less with frequency than the impedance between the electrodes to the Ten20 paste. The impedance between the two cup electrodes is so low that it prevents high spatial resolution since it almost shorts the circuit out. We also found that the phase of the TCRE is flatter from 1 to 100 Hz than the phase of the cup electrode. This would be beneficial when conducting a phase analysis.

Equations 3-4, 8-10, 12, 20 in section III, showed the relationship of the electrode parameters to the electrode type, the area, the electrolyte, the frequency and the current density. This is also proven by the experimental data shown in Figures 7-13. For the TCRE, the central disc has the lowest surface area and the plot in Fig. 9 depicts that it has the highest impedance compared to the middle and outer rings. On the other hand, the outer ring has the highest surface area, and the plot in Fig. 11 illustrates that it has the lowest impedance. Moreover, since the cup electrode has larger surface area than the elements of the TCRE, the plot in Figures 12-13 shows that it has less impedance than the TCRE. The proposed model of Fig. 6 depicts that at higher frequencies the impedance of the double layer capacitor, C_d, becomes so small and shorts the part of the model in parallel to it. However, the model shows that the impedance between the rings would be limited to R_{soln}. The value of the R_{soln}, as shown in Table I, is about 300Ω at approximately $1kHz$, not a short.

Furthermore, our experiment showed that the response in the ABR can be detected reliably with only 500 stimuli by using tripolar concentric ring electrodes. The standard number of stimuli is 2000 to detect the ABR by conventional electrode signal averaging [19]-[21]. In particular, for hearing screening of newborns the number of stimuli should be kept to a minimum. Therefore, detecting the ABR by fewer trials offers a great advantage of TCREs. If only the wave V is needed, then it is likely possible to complete the hearing test using tEEG with 500, or less, audio stimuli.

Acknowledgment

The authors would like to thank Dr. Richard Brown for allowing us to use the Gamry potentiostat.

References

[1] L. A. Geddes and L. E. Baker, *Principles of applied biomedical instrumentation*. John Wiley & Sons, 1989.

[2] C. Boccaletti et al., "A non-invasive biopotential electrode for the correct detection of bioelectrical currents," in *Proceedings of the Sixth IASTED International Conference on Biomedical Engineering*, pp. 353–358, ACTA Press, 2008.

[3] H. Wang and L. Pilon, "Accurate simulations of electric double layer capacitance of ultramicroelectrodes," *The Journal of Physical Chemistry C*, vol. 115, no. 33, pp. 16711–16719, 2011.

[4] L. Geddes, "Historical evolution of circuit models for the electrode-electrolyte interface," *Annals of biomedical engineering*, vol. 25, no. 1, p. 1, 1997.

[5] G. Besio et al., "Tri-polar concentric ring electrode development for laplacian electroencephalography," *IEEE transactions on biomedical engineering*, vol. 53, no. 5, pp. 926–933, 2006.

[6] K. Koka and W. G. Besio, "Improvement of spatial selectivity and decrease of mutual information of tri-polar concentric ring electrodes," *Journal of neuroscience methods*, vol. 165, no. 2, pp. 216–222, 2007.

[7] S. H. Nasrollaholhosseini et al., "Electrode-electrolyte interface model of tripolar concentric ring electrode and electrode paste," in *Engineering in Medicine and Biology Society (EMBC), 2016 IEEE 38th Annual International Conference of the*, pp. 2071–2074, IEEE, 2016.

[8] S. H. Nasrollaholhosseini et al., "Impedance spectroscopy of tripolar concentric ring electrodes with ten20 and td246 pastes," in *Engineering in Medicine and Biology Society (EMBC), 2017 39th Annual International Conference of the IEEE*, pp. 2426–2429, IEEE, 2017.

[9] A. R. Korshoej et al., "Importance of electrode position for the distribution of tumor treating fields (ttfields) in a human brain. identification of effective layouts through systematic analysis of array positions for multiple tumor locations," *PloS one*, vol. 13, no. 8, p. e0201957, 2018.

[10] H. Azizollahi et al., "Effects of uncertainty in head tissue conductivity and complexity on eeg forward modeling in neonates," *Human brain mapping*, vol. 37, no. 10, pp. 3604–3622, 2016.

[11] J. E. Desmedt et al., "Emulation of somatosensory evoked potential (sep) components with the 3-shell head model and the problem of 'ghost potential fields' when using an average reference in brain mapping," *Electroencephalography and Clinical Neurophysiology/Evoked Potentials Section*, vol. 77, no. 4, pp. 243–258, 1990.

[12] P. Nunez et al., "A theoretical and experimental study of high resolution eeg based on surface laplacians and cortical imaging," *Electroencephalography and clinical neurophysiology*, vol. 90, no. 1, pp. 40–57, 1994.

[13] N. Joye et al., "Electrical modeling of the cell–electrode interface for recording neural activity from high-density microelectrode arrays," *Neurocomputing*, vol. 73, no. 1-3, pp. 250–259, 2009.

[14] W. Franks et al., "Impedance characterization and modeling of electrodes for biomedical applications," *IEEE Transactions on Biomedical Engineering*, vol. 52, no. 7, pp. 1295–1302, 2005.

[15] T. Jochum et al., "Integrated circuit amplifiers for multi-electrode intracortical recording," *Journal of neural engineering*, vol. 6, no. 1, p. 012001, 2009.

[16] B. Hirschorn et al., "Constant-phase-element behavior caused by resistivity distributions in films i. theory," *Journal of The Electrochemical Society*, vol. 157, no. 12, pp. C452–C457, 2010.

[17] J.-h. Chang et al., "Fitting improvement using a new electrical circuit model for the electrode-electrolyte interface," in *Neural Engineering, 2007. CNE'07. 3rd International IEEE/EMBS Conference on*, pp. 572–574, IEEE, 2007.

[18] E. Gongadze et al., "Classical models of the interface between an electrode and an electrolyte," in *COMSOL Conference*, pp. 14–16, 2009.

[19] R. Zhang et al., "Combining wavelet analysis and bayesian networks for the classification of auditory brainstem response," *IEEE Transactions on Information Technology in Biomedicine*, vol. 10, no. 3, pp. 458–467, 2006.

[20] J. H. Kim et al., "An electroplating-free and minimal noise polyimide microelectrode for recording auditory evoked potentials from the epicranius," *IEEE Transactions on Biomedical Engineering*, vol. 60, no. 12, pp. 3425–3431, 2013.

[21] J. Krizman et al., "Stimulus rate and subcortical auditory processing of speech," *Audiology and Neurotology*, vol. 15, no. 5, pp. 332–342, 2010.